Computational Materials Science 83 (2014) 426–433

Contents lists available at ScienceDirect

Computational Materials Science

journal homepage: www.elsevier.com/locate/commatsci

XTRANS: An electron transport package for current distribution and magnetic field in helical nanostructures

Fangbo Xu [a], Arta Sadrzadeh [a], Zhiping Xu [b], Boris I. Yakobson [a,*]

[a] Department of Mechanical & Materials Science, Rice University, Houston, TX 77251, USA
[b] Department of Engineering Mechanics, Tsinghua University, Beijing 100084, China

ARTICLE INFO

Article history:
Received 13 October 2013
Received in revised form 19 November 2013
Accepted 23 November 2013

Keywords:
Electron transport
Magnetic field
Helical symmetry
Non-equilibrium Green's function

ABSTRACT

In this paper, the algorithms of non-equilibrium Green's function (NEGF) approach for electron transport properties of nanostructures which are implemented in XTRANS, the package developed by our group, are described. Incorporated with the tight-binding method, this package not only can compute the regular PBC structure, but also is capable of studying those systems which possess no translational symmetry but helical symmetry. It selects the appropriate symmetry to minimize the computation cost if the system is subject to both symmetries. It also involves the utility of visualizing the current distribution across the nanostructure in forms of "bond current", with which we developed a fast and accurate procedure to compute the induced magnetic field and further the inductance. To demonstrate the application, we also calculate multiple examples of nanostructures with either translational or helical symmetry, and reveal their distinctive electric and magnetic properties. To our knowledge, these features have never been available in previous ready-to-use packages for electron transport.

1. Introduction

The development tendency of electronic devices is smaller, faster but less dissipation. The ongoing miniaturization of microelectronic devices has advanced to the scale of nanometers during the past decades, and current lithographic techniques are able to manufacture ~10 nm heterostructure of semiconductors [1–4]. In addition, many low-dimensional materials, such as carbon nanotubes (CNT), graphene, boron sheet, and MoS_2, have spurred a surge of research interest regarding their novel properties in mechanics and electronic structures [5–18]. Moreover, even single molecules are employed to fabricate electronic devices with the ultimate size [19–25]. In these transport systems, the number of carriers is dramatically reduced so that quantization of charges becomes significant [26–30]. Meanwhile, the motion of electrons is confined in at least one dimension, and the phase coherence as well as the energy is preserved during the transport process, as demonstrated by the quantized conductance and negative differential resistance observed in experiments [31,32]. As a result, the scattering of electrons occurs in the presence of the potential of nuclei and other electrons, and accordingly the particular electronic structure as well as the atomistic details of contacts has to be taken into account explicitly to study the electron transport properties of nanoscale devices.

As far as the theoretical research regarding electron transport is concerned, numerous works have been presented on different levels of approximation to the electronic structure, ranging from model Hamiltonian (e.g. π-electron tight-binding method of fullerene [33]), to the first-principle calculation, in which the density functional theory (DFT) is prevailingly used [34–36]. When the Hamiltonian is determined, the transport calculation may proceed in two distinctive ways: one is to solve the wavefunctions and transmission probabilities of scattering states with the Lippmann–Schwinger equation, and then the current can be computed by summing up the contribution of the occupied scattering states in each electrode [37]. This method is usually prohibitively expensive and turns out intractable on large systems. The more practical approach is based on the non-equilibrium Green's function formalism (NEGF), which usually comes in matrix form [38–41]. The NEGF approach substitutes the motion equation of Green's function into the current operator of each electrode and thus obtain the exact expressions of current and conductance, by which, under the ballistic assumption, one can readily obtain the transmission coefficient of Bloch waves as well as the total current, according to the Landauer formula [42]. Moreover, the Green's functions are related to the wavefunctions of the scattering states through the spectral representation [39,43], implying that we can extract from the NEGF procedure more information concerning the physical quantities well-defined in a particular state of the system, such

* Corresponding author. Address: MEMS Dept., MS 321, Rice University, 6100 Main St., Houston, TX 77005-1892, USA. Tel.: +1 713 348 3572; fax: +1 713 348 5423.
E-mail address: biy@rice.edu (B.I. Yakobson).

0927-0256/$ - see front matter © 2013 Elsevier B.V. All rights reserved.
http://dx.doi.org/10.1016/j.commatsci.2013.11.043

as spatial distributions of electron density, electrostatic potential, and current density, which are of great interest in the research of electronic properties and also serve as the basis of comprehensive analysis for diverse nanoscale devices and materials.

In this work, we present the algorithm of calculating the magnetic field and the inductance of atomistic transport systems, based on the "bond-current" approximation within the framework of NEGF formalism. Bond-current approach assumes that the electric current flows from atom to atom via their chemical bonding [44,45], serving as a useful tool for visualization of current distribution and fast computation for the induced magnetic field. We first describe the general formalism of NEGF approach in matrix form and the exact expression for current density. Second, the derivation of bond-current for the orthogonal basis set in conjunction with Green's functions is briefly depicted. Finally we present the procedure which computes the magnetic field and inductance of some nanostructures by combining the bond current and the exact current density so as to overcome the divergence while applying the Biot-Savart law. These algorithms have been implemented in the package named XTRANS developed by our group, with which we are able to explore electric and magnetic properties of various nanostructures.

2. Formulation

2.1. The General formalism of the NEGF approach

Here we briefly describe the general formalism of the NEGF approach, in conjunction with either quantum chemical computation like DFT, or model Hamiltonian obtained by the tight-binding (TB) method. The computation for Hamiltonian should be performed in a finite basis set constituted by localized atomic orbitals, so that the whole system could be divided into different regions: leads and device. Each of the leads is constructed as a semi-infinite PBC structure with a unit cell large enough so that only the neighboring unit cells possess non-trivial Hamiltonian (H) and overlap (S) elements. These supercells are sometimes referred as "principle layers". The device region usually includes several principle layers of each lead, assuming that the outmost ones which are immediately connected to the lead possess the same H and S elements as in the deep lead. Meanwhile the distance between the leads should be sufficiently large so as to eliminate the interaction between them.

Let us consider a two-terminal open system which is divided into three parts: left lead (L), device (D) and right lead (R). The Green's function equation for the entire system can be written in matrix form as follows:

$$(zS-H)G=\begin{pmatrix} zS_L-H_L & \tau_L^\dagger & 0 \\ \tau_L & zS_D-H_D & \tau_R \\ 0 & \tau_R^\dagger & zS_R-H_R \end{pmatrix}\begin{pmatrix} G_L & G_{LD} & G_{LR} \\ G_{DL} & G_D & G_{DR} \\ G_{RL} & G_{RD} & G_R \end{pmatrix}=I \tag{1}$$

where $z = E + i\eta$, $\eta \to 0^+$. $\tau_{L/R}$ describes the coupling of the device with the left/right lead. Multiplying all the rows of the first matrix with the 2nd column of the second matrix and solving for G_D, one obtains:

$$G_D(E) = (zS_D - H_D - \Sigma_L - \Sigma_R)^{-1} \tag{2}$$

where $\Sigma_{L/R} = \tau_{L/R} g_{L/R} \tau_{L/R}^\dagger$, named self-energy, represents the influence of leads on the device, and $g_{L/R} = (zS_{L/R} - H_{L/R})^{-1}$ is called surface Green's function (SGF), corresponding to the semi-infinite leads, which can be solved by a recursive procedure as discussed in Appendix I. With G_D and $\Sigma_{L/R}$, the transmission coefficient for a given energy can be written as:

$$\begin{aligned} T(E) &= Tr[\Gamma_L G_D \Gamma_R G_D^\dagger], \\ \Gamma_{L/R} &= i\left(\Sigma_{L/R} - \Sigma_{L/R}^\dagger\right) \end{aligned} \tag{3}$$

Then the total current of the transport system is obtained by Landauer formula:

$$I = \frac{2e}{h}\int_{-\infty}^{\infty} T(E)[f_L(E) - f_R(E)]\,dE \tag{4}$$

where $f_{L/R}(E)$ is the Fermi–Dirac function of either lead.

Additionally, the Green's function also can be expressed in terms of wavefunctions of the system and thus it can help compute some quantities regarding the states of electrons. For instance, the charge density $n(\vec{r},t)$ can be determined in terms of the "lesser" Green's function $G^<$ [38,46]:

$$n(\vec{r},t) = -iG^<(\vec{r},t;\vec{r},t) = \left\langle \psi^\dagger(\vec{r},t)\psi(\vec{r},t)\right\rangle \tag{5}$$

Plugging the Schrödinger equation with respect to $\psi(\vec{r},t)$ into the time derivative of $n(\vec{r},t)$, taking into account the conservation of charge $\frac{\partial n(\vec{r},t)}{\partial t} = -\nabla\cdot j(\vec{r})$, we can obtain the expression for current density:

$$\begin{aligned} \boldsymbol{J}(\vec{r}) &= \frac{\hbar}{2m_e}\lim_{\vec{r}\to\vec{r}'}(\nabla' - \nabla)G^<(\vec{r},\vec{r}') \\ &= \frac{\hbar}{2m_e}\sum_{ij}\int G_{ij}^<(E)\lim_{\vec{r}\to\vec{r}'}(\nabla' - \nabla)\phi_i(\vec{r})\phi_j^*(\vec{r}')dE \end{aligned} \tag{6}$$

where $\{\phi_i(\vec{r})\}$ is the basis set of atomic orbitals. In matrix form $G^<$ can be computed by [38,47]:

$$G^<(E) = i[G_D\Gamma_L G_D^\dagger]f_L + i[G_D\Gamma_R G_D^\dagger]f_R \tag{7}$$

2.2. Bond current

In most cases the computation of current density behaves too demanding. Here we employ another approach regarding the current distribution which implements the concept of "bond current" [44,45]. By calculating the change rate of electron occupation on each atomic site, one finds that this change rate is contributed by the non-trivial Hamiltonian elements which correspond to the chemical bonds of this atom with its neighbors. Therefore we assume a "bond current" flowing through each atomic bond.

Under an orthogonal basis set $\{|\varphi_{n\gamma}\rangle\}$, where n denotes atom and γ labels the orbitals at n, we define a projection operator:

$$\hat{P}_n = \sum_\gamma |\varphi_{n\gamma}\rangle\langle\varphi_{n\gamma}| \tag{8}$$

$\hat{P}_n$ describes the occupation of the atomic site n. Then the change rate of the occupation is evaluated as:

$$\hat{I}_n = \frac{d}{dt}\hat{P}_n = \frac{1}{i\hbar}\left[\hat{P}_n, \hat{H}\right] \tag{9}$$

Taking into account the completeness of $\{|\varphi_{n\gamma}\rangle\}$: $\sum_n \hat{P}_n = 1$, and assuming the current at the atomic site n comes from or goes to other sites n', we obtain

$$\hat{I}_n = \sum_{n'}\hat{I}_{n'n} = \sum_{n'}\frac{1}{i\hbar}\left(\hat{P}_n\hat{H}\hat{P}_{n'} - \hat{P}_{n'}\hat{H}\hat{P}_n\right) \tag{10}$$

Therefore $\hat{I}_{n'n} = \frac{1}{i\hbar}\left(\hat{P}_n\hat{H}\hat{P}_{n'} - \hat{P}_{n'}\hat{H}\hat{P}_n\right)$ is considered as the bond current between atomic sites n' and n. To solve the expectation value of $\hat{I}_{n'n}$, we perform:

$$I_{n'n} = eTr\left[\hat{I}_{n'n}\hat{\Omega}(V)\right] \tag{11}$$

where $\hat{\Omega}$ is the density operator and V is the voltage. If we use $D_L(E)$ to denote the density operator at the energy E arising from the incoming Bloch wave from the left lead, it gives [44]:

$$I_{n'n} = e\int dE[f_L(E) - f_R(E)]Tr[\hat{I}_{n'n}D_L(E)] \tag{12}$$

and $D_L(E)$ is evaluated by (see Appendix II for derivation)

$$D_L = \frac{1}{2\pi}G_D\Gamma_L G_D^{\dagger} \tag{13}$$

If we include the spin-degeneracy factor of 2, one obtains:

$$\begin{aligned} I_{n'n} &= \frac{2e}{i\hbar}\sum_{\gamma\gamma'}\int_{\mu_R}^{\mu_L}\left[H_{n\gamma n'\gamma'}D_L(E)_{n'\gamma' n\gamma} - (n \leftrightarrow n')\right]dE \\ &= \frac{4e}{\hbar}\sum_{\gamma\gamma'}\int_{\mu_R}^{\mu_L}\mathrm{Im}\left[H_{n\gamma n'\gamma'}D_L(E)_{n'\gamma' n\gamma}\right]dE \end{aligned} \tag{14}$$

where μ_L and μ_R are the Fermi levels of the left and right leads, respectively. These results imply that only the incoming Bloch waves between μ_L and μ_R ($\mu_L > \mu_R$) from the left lead contribute to the total current while the incoming waves from the right lead are canceled out. Note that the bond-current operator only works for the orthogonal orbitals while for non-orthogonal orbitals, so far no Hermitian projection operator like Eq. (8) can be defined. Possible strategy may involve searching for appropriate hopping parameters for the orthogonal orbitals which could reproduce DFT electronic structures for more complex nanostructures, and specific schemes have been discussed in previous literature [48,49].

2.3. Conductance computation for helical symmetry

The energetics and electromechanics of various nanostructures with helical symmetry have been developed [50–56] and later [57–68]. While mostly the band structure was considered, the NEGF approach, which is commonly used for translational symmetry, was barely implemented, and the spatial current distribution was not available, excluding the possibility of inductance analysis. In what follows we describe a scheme that mathematically converts the Hamiltonian of a helically symmetric system such that the standard NEGF approach can be applied.

In most cases of electron transport calculation, the electrodes comprises of unit cells with translational symmetry, and correspondingly the H and S matrices are block-diagonal and exhibit the PBC feature:

$$\begin{aligned} &H_{00} = H_{11} = \cdots = H_{nn}, H_{01} = H_{12} = \cdots H_{nn+1}, \\ &S_{00} = S_{11} = \cdots = S_{nn}, S_{01} = S_{12} = \cdots S_{nn+1} \end{aligned} \tag{15}$$

where n and $n+1$ label two neighboring unit cells, respectively. This is the foundation upon which the surface Green's functions are calculated (see Appendix I). In some systems with helical symmetry [53,69], however, their H and S matrices do not carry the PBC feature. For instance, as shown in Fig. 1, A and B are both helical unit cells (HUC). B can be obtained by rotating A by an angle of θ with respect to the z axis perpendicular to the paper plane, plus a displacement along the z direction. To our knowledge, most of the quantum chemistry packages usually give the H and S matrices based on the standard atomic orbitals which are defined with respect to the three coordinate axes. As far as the bonding of p_x orbitals is concerned, in A the p_x orbitals form the $pp\sigma$ bond, which though does not hold for the p_x orbitals in B, but instead a hybrid $pp\sigma + pp\pi$ bond comes into play. As a result, $H_{AA} \neq H_{BB}, S_{AA} \neq S_{BB}$, and therefore the NEGF approach above is no longer applicable. Nevertheless, if we rotate the initial p_x orbitals in B to form a new orbital p'_x, which is oriented along the connecting line between the atoms, then the $pp\sigma$ bond is recovered. The argument also applies on the bonding of p_y orbitals while p_z remains invariant after the rotation. The new basis set can be obtained by linear combination of the old one, and some of the corresponding coefficients $\left\langle \phi^{(\theta)}|\phi \right\rangle$ commonly used are summarized in Table 1, where $\phi^{(\theta)}$ notates a rotated atomic orbital and θ is the angle it sweeps during the rotation.

Under the new basis set, the diagonal blocks of H and S matrices for each HUC become equal, while the off-diagonal blocks between neighboring HUCs are also consistent because of the identical relative positions. Accordingly the PBC feature of H and S matrices is retrieved, and the NEGF approach suitable for PBC structure becomes applicable to helical-symmetric systems, such as chiral CNTs and twisted graphene nanoribbons [64–67,70]. Moreover, for some systems with both translational and helical symmetries (e.g. chiral CNTs), taking advantage of helical symmetry may require smaller unit cells and thus significantly reduce the cost of computation.

Our XTRANS package incorporates the H and S matrices that are evaluated by TROCADERO code which implements the non-orthogonal tight-binding method with Slater–Koster integrals [71–73]. In the following section we will show some examples to demonstrate the capability of XTRANS in analyzing the electric properties of various nanoscale systems.

3. Applications

3.1. Current distribution of carbyne

The monatomic carbon chain, also known as carbyne, recently has attracted amount of attention due to its outstanding mechanical properties [74–76]. Also it serves as the simplest system in which the current distribution of a C–C bond could be studied, as illustrated in Fig. 2(a). The distribution exhibits axially symmetric with respect to the axis of carbyne, and the color rings plotted on the cross-section indicate the vanished magnitude at the axis as well as the maximum around the atomic radius. This is consistent with the known fact that the localized σ bonds only constitute the skeleton of atomic structure while the delocalized π bonds account for the electric current. Referring to the equations for the wavefunctions of carbon atoms, the radial distribution of the current density carried by each C–C bond can be fitted by:

$$J(r) = 61.64I_0r^3e^{-6.22r} \tag{16}$$

where r is the radial coordinate in unit of Å and I_0 is the value of bond current.

Next we intend to calculate the induced static magnetic field. In principle, for a given current density field $J(\vec{r})$, the vector potential field $\vec{A}(\vec{r}) = \frac{\mu_0}{4\pi}\int\frac{J(\vec{r}')d\vec{r}'}{|\vec{r}-\vec{r}'|}$ should be computed first and then the magnetic field can be solved as $\vec{B} = \nabla \times \vec{A}$. This method is quite expensive since it involves double integrations of the entire meshgrid.

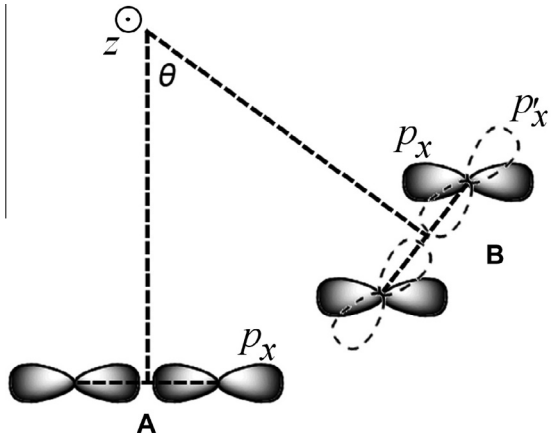

Fig. 1. The schematic view of bonding of p_x orbitals in any two neighboring helical unit cells.

Table 1
The coefficients of linear combination for the transformation of the old basis set into the rotated one. Only the non-trivial are listed. The rotation is with respect to the z axis.

	s	p_x	p_y	p_z	d_{xy}	d_{xz}	d_{yz}	$d_{x^2-y^2}$	d_{z^2}
$s^{(\theta)}$	1								
$p_x^{(\theta)}$		$\cos\theta$	$\sin\theta$						
$p_y^{(\theta)}$		$-\sin\theta$	$\cos\theta$						
$p_z^{(\theta)}$				1					
$d_{xy}^{(\theta)}$					$\cos 2\theta$			$-\sin 2\theta$	
$d_{xz}^{(\theta)}$						$\cos\theta$	$\sin\theta$		
$d_{yz}^{(\theta)}$						$-\sin\theta$	$\cos\theta$		
$d_{x^2-y^2}^{(\theta)}$					$\sin 2\theta$			$\cos 2\theta$	
$d_{z^2}^{(\theta)}$									1

Another approach takes each of the bond currents as a breadthless conducting wire and therefore the magnetic field can be solved in an analytical way, although $\vec{B}(\vec{r}) \to \infty$ when it comes close to the bonds. To circumvent this problem we utilize the current density of the carbyne and assume each of the bond currents carries such distribution as presented by Eq. (16). Only the coefficient A needs to be altered for different values of the bond current. Each bond current is divided into a bunch of conducting wires and the magnetic field induced by each of them can be solved analytically. Finer partitioning is executed until the result converges. This procedure avoids the divergence occurring at the meshgrid points close to or inside the chemical bonds, and reasonably gives rise to the magnetic field that accords with that of a breadthless conducting wire at the region far from the bonds.

Fig. 2(b) shows the induced static magnetic field that is evaluated by applying the scheme discussed above. The distribution of magnitude shares the similar pattern with the current density. Fig. 2(c) displays the corresponding radial distributions of the current field and the magnetic field. The black curve is calculated by way of the approach described above, while the blue curve is obtained by simply applying Biot-Savart law to a breadthless conducting wire. We see that, our approach eliminates the singularities and the resulting magnetic field varies continuously over space, and when it is far enough from the bond axis, the bond current reasonably tends to be a breadthless wire carrying current.

The availability of the magnetic field allows us to calculate the magnetic flux vs. current and further the inductance. We estimate the effective radius r_{eff} of carbyne as a classical conductor. For a conducting cylinder in which the current density uniformly distributes, the magnetic flux per length through the surface (yellow) shown in Fig. 2(b) is

$$\Phi = \frac{\mu_0}{2\pi}\left(\frac{1}{2} + \ln\frac{R}{r_0}\right)I \tag{17}$$

where r_0 is the radius of the cylinder. Our results for carbyne suggests that Φ is linearly dependent on I with a varying slope for different given values of R, while r_0 remains invariant all the time. Accordingly, the effective radius of carbyne is found to be $r_{eff} = \langle r_0 \rangle = 1.20$ **Å**.

3.2. Chiral carbon nanotubes

As is known a chiral CNT exhibits both translational and helical symmetries [53,55]. The translational unit cell usually contains more atoms than the helical unit cell, but the physical properties should be consistent when we make use of either of the symmetries. We take (6,3) CNT for example to demonstrate the validity of our NEGF algorithm for helical symmetry. Fig. 3(a) shows the translational unit cell of (6,3) CNT which contains 84 atoms, as well

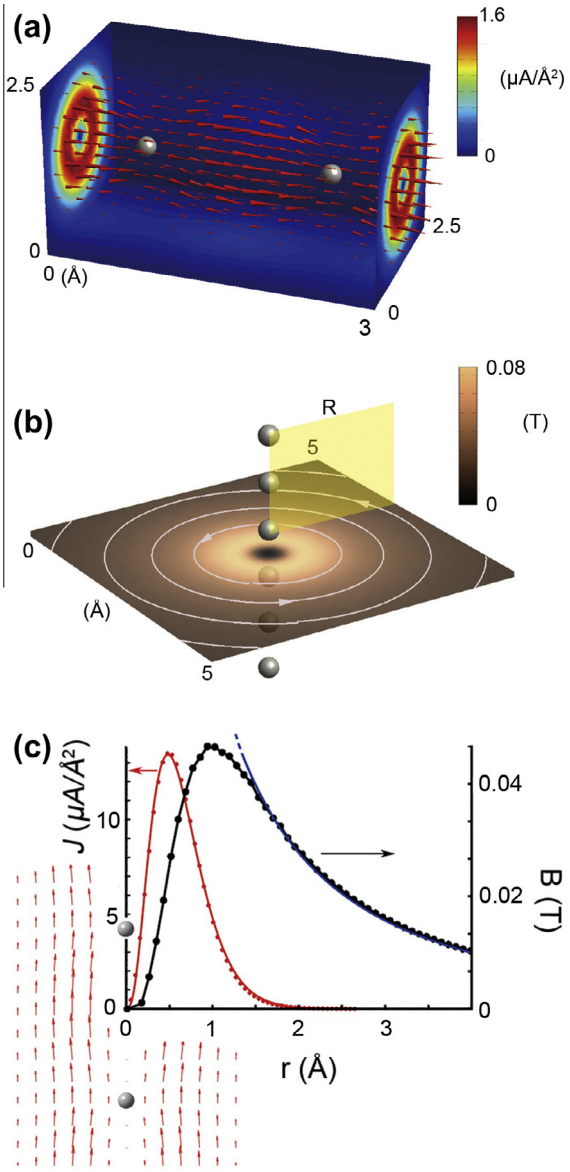

Fig. 2. (a) Current density distribution of a monoatomic carbon chain, under a voltage of 0.5 V. (b) The static magnetic field induced by the current density field of (a). (c) The vector field of the current density distribution over a middle section of a carbon monoatomic chain, as well as the induced magnetic field. The red curve presents the radial distribution of the current density. The black curve represents the radial magnetic field using bond current approximation, and the blue curve is obtained by regarding the bond current as a breadthless wire. The value of the bond current is set to be $1e^2/h$. (For interpretation of the references to colour in this figure legend, the reader is referred to the web version of this article.)

as the corresponding band structure, suggesting that the (6,3) tube is essentially metallic but a band gap emerges due to the significant curvature. Here the k-vector is defined to orient along the direction of translation. The upper panel of Fig. 3(b) depicts the HUC (highlighted) containing only 12 atoms, and the rotation angle and displacement between neighboring HUCs are 154.286 degrees and 3.0 Å, respectively. The "helical band structure" and the conductance as a function of energy are shown in the lower left and right panels of Fig. 3(b), respectively. In this case the wave vector κ is different from the translational k. Both of the band structures display the same band gap and result in the equal conductance over the entire energy region. In that sense employing helical symmetry provides the correct electrical properties of the system with significantly reduced computation cost. Note that although the

minimum HUC contains 3 dimers and is much smaller than what we use, we have to select an appropriate size of HUC which is sufficiently large to ensure the corresponding H and S matrices are block-tridiagonal.

3.3. Wrapped graphene nanoribbons

Now we turn to the zigzag-edged graphene nanoribbon (ZGNR) which is wrapped on the surface of a cylinder. In this system the helical symmetry prevails and the translational symmetry appears only when $2\pi m$ (m is an integer) can be divided exactly by the angle shift between the neighboring HUCs. The upper panel of Fig. 4(a) shows the structure of a ZGNR with 6 rows of zigzag chains, wrapped around the cylinder with a radius of 6.0 Å, and the red rectangle marks the HUC which contains 12 carbon atoms. The rotation angle and displacement between neighboring HUCs are $\theta = 21^\circ$ and $dz = 1.29$ Å, respectively. Our calculation suggests the electric properties (e.g. band structure) are not sensitive to (θ, dz) unless the radius of the imaginary cylinder is less than 3.0 Å. The lower panel of Fig. 4(a) presents the helical band structure (left) computed with the non-orthogonal TB method, as well as the curve of conductance vs. energy calculated by NEGF approach (right). The curve of conductance agrees with that of a flat ZGNR, indicating the electric properties of ZGNR are robust when the curvature is not significant. Since our TB method does not involve spin-polarization, part of the band structure exhibits nearly flat at the Fermi level and thus accounts for the peak of conductance at the Fermi level, as reported by previous literature [77,78].

In order to study the current distribution of the wrapped ZGNR, we implement the bond-current algorithm described in Section 2, with the orthogonal π-orbital TB + NEGF method. The hopping parameters for the nearest and the second nearest neighboring carbon atoms are −2.75 eV and 0.069 eV, respectively [79]. The calculated conductance agrees with what is shown in Fig. 3(a) except that the sharp peak at the Fermi level is absent. By implementing Eq. (14), we plot the position-resolved distribution of electric current at each atomic site, which is shown in Fig. 4(b). The voltage is set to be 0.5 V, implying an integration over the yellow[1] energy window marked in Fig. 3(a). The direction of the current on the atomic site α is defined as $\vec{i}_\alpha = \frac{1}{2}\sum_\beta I_{\alpha\beta}\vec{e}_{\alpha\beta}$, where $I_{\alpha\beta}$ is the bond current between α and β and $\vec{e}_{\alpha\beta}$ is the unit directional vector from α to β. This definition works for the carbyne and graphene nanoribbons [80]. Fig. 4(b) suggests that the current is continuous in the direction of transport but the distribution is not uniform across the strip: the magnitude at the edges is suppressed while it bulges in the interior region. This observation agrees with the results for the flat ZGNR reported in the previous literature [80]. Comparing with current density distribution, [cf. Fig. 2(a)], which excessively depends on the spatial coordinates of the meshgrid, the pattern formed by bond currents [cf. Fig. 4(b)] serves as a more straightforward recipe for visualization of the current distribution across the atomic structure.

Fig. 4(c) presents the magnetic field on the cutting plane which goes through the axis of the wrapped ZGNR, induced by the collection of all the bond currents which possess the presumed current density distribution as Eq. (16). As illustrated in the figure, the magnetic field is mostly concentrated in the cavity wrapped by the strip. On the other hand, due to the peculiar distribution of current and loose arrangement of turns, the magnetic leakage becomes considerable while the magnetic vectors inside the cavity are no longer oriented along the z direction uniformly and the magnitude is much lower than that of an ideal solenoid. In addition, we compute the magnetic flux through the cross section, as

[1] For interpretation of color in Fig. 3, the reader is referred to the web version of this article.

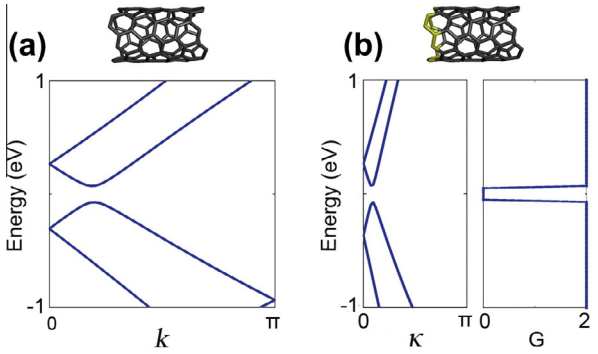

Fig. 3. (a) The side view of the translational unit cell of (6,3) CNT and the band structure of translational symmetry. (b) Upper panel: the side view of the helical unit cell of (6,3) CNT (highlighted); lower panel: the "band structure" of helical symmetry (left) and the conductance around the Fermi level (right).

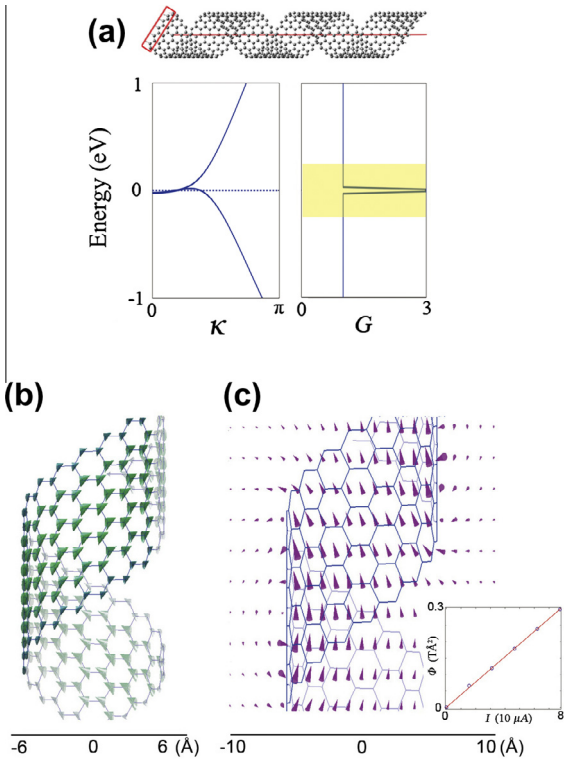

Fig. 4. (a) The side view of the ZGNR ($N_{zz} = 6$) wrapped on the surface of an imaginary cylinder, and the conductance around the Fermi level. The unit of the conductance is $2e^2/h$. (b) The current distribution of the ZGNR under a voltage of 0.5 V. The size of the arrow heads corresponds to the magnitude of the current on individual atoms which are scaled to the maximum of 0.16 mA. (c) The magnetic field on the cutting plane through the axis of the ZGNR. The size of the arrow heads correspond to the magnitude scaled to the maximum of 57 gauss. The inset displays the linear dependence of the magnetic flux through the cross-section on the total current.

shown in the inset of Fig. 4(c), from which the inductance for a single turn is found to be 3.8×10^{-2} fH.

4. Conclusion

In this paper we present various approaches of modeling the electric and magnetic properties of current-carrying nanoscale systems, which have been implemented in our atomistic simulation package XTRANS. We have discussed the standard formalism of the NEGF approach, with which we employ the bond-current approach developed by Todorov, exclusively combined with the

orthogonal TB approach. The bond currents could provide position-resolved distribution of electric current across the nanostructure with a reasonable volume of computation. In contrast to the current density derived from $G^<$, the bond-current approach reveals the current carried by each chemical bond so that bypasses expensive computation such as derivative of wavefunctions of all the relevant atomic orbitals, as well as unnecessary information like what happens inside the chemical bonds. By combining bond currents with the approximation for the distribution of current density for a single chemical bond, we can estimate the induced magnetic field with good accuracy while avoiding the singularities in the vicinity of the chemical bonds. In the region which is far away from chemical bonds, for instance, the cavity of a solenoid formed by a strip of ZGNR, most of the bond currents behave as breadthless conducting wires so that the magnetic field can be solved analytically and efficiently.

We have also discussed the way in which the system of helical symmetry is converted by the transformation of the basis set so as to assure that the transformed H and S matrices possess the PBC feature. This scheme not only allows the electron transport properties of helical-symmetry systems to be calculated within the common framework of the NEGF approach, but also may greatly shrink the volume of computation if the system bears both symmetries. Such treatment, combined with the H and S matrices obtained from non-orthogonal TB or DFT method, extends the usage of the NEGF approach and thus provides the means to perform comprehensive simulation and analysis on various current-carrying nanoscale systems.

Acknowledgements

This work was supported by the National Science Foundation CMMI Grant #0951145 (EAGER) and in part by the US Air Force Office of Scientific Research Grant FA9550-12-1-0035 (MURI).

Appendix A

A.1. Surface Green's function (SGF)

Referring to the self-energy $\Sigma_{L/R} = \tau_{L/R} g_{L/R} \tau_{L/R}^\dagger$, $g_{L/R} = (zS_{L/R} - H_{L/R})^{-1}$ literally represents the Green's function of the entire lead, but it proves to be impractical to calculate the inverse matrix of this semi-infinite matrix in real calculations. Nevertheless, in simulations $\tau_{L/R}$ usually describes the interaction of the device with the principle layers of the lead that are immediately connected to the device, instead of the whole lead, and hence what really matters in $g_{L/R}$ is no more than the block corresponding to those principle layers, namely G_{00}. That's why it is called "surface".

There are many ways to derive the formalism of SGF [38,81–83]. Here we present one of them [83]. We assume our one-dimensional PBC lead is oriented horizontally, and the unit cells are sufficiently large so that only the neighboring unit cells possess non-trivial H and S elements, while H_{01} and S_{01} represent the blocks between a unit cell and its right-hand-side neighbor. As far as the right lead is concerned, from the definition of matrix Green's function we have

$$\begin{pmatrix} zS_{00}-H_{00} & zS_{01}-H_{01} & & \\ zS_{01}^\dagger-H_{01}^\dagger & zS_{00}-H_{00} & zS_{01}-H_{01} & \\ & zS_{01}^\dagger-H_{01}^\dagger & zS_{00}-H_{00} & \ddots \\ & & \ddots & \ddots \end{pmatrix} \begin{pmatrix} G_{00} & G_{01} & G_{02} & \\ G_{10} & G_{11} & G_{12} & \cdots \\ G_{20} & G_{21} & G_{22} & \\ & \cdots & & \end{pmatrix} = I \quad (18)$$

where $z = E + i\eta$, $\eta \to 0^+$. Multiplying all the rows of the first matrix with the 1st column of the second matrix, it gives

$$\begin{aligned} &(zS_{00} - H_{00})G_{00} = 1 + (H_{01} - zS_{01})G_{10} \\ &(zS_{00} - H_{00})G_{10} = (H_{01}^\dagger - zS_{01}^\dagger)G_{00} + (H_{01} - zS_{01})G_{20} \\ &\vdots \\ &(zS_{00} - H_{00})G_{n0} = (H_{01}^\dagger - zS_{01}^\dagger)G_{n-1,0} + (H_{01} - zS_{01})G_{n+1,0} \end{aligned} \quad (19)$$

Here we take advantage of the PBC feature of the H and S matrices:

$$\begin{aligned} &H_{00} = H_{11} = \cdots = H_{nn}, H_{01} = H_{12} = \cdots H_{nn+1}, \\ &S_{00} = S_{11} = \cdots = S_{nn}, S_{01} = S_{12} = \cdots S_{nn+1} \end{aligned}$$

Then we obtain the general expression for G_{n0}:

$$\begin{aligned} G_{n0} &= (zS_{00} - H_{00})^{-1}\left[\left(H_{01}^\dagger - zS_{01}^\dagger\right)G_{n-1,0} + (H_{01} - zS_{01})G_{n+1,0}\right] \\ &= t_0 G_{n-1,0} + \tilde{t}_0 G_{n+1,0} \end{aligned} \quad (20)$$

Applying recursively, one obtains:

$$\begin{aligned} G_{n0} &= t_i G_{n-2^i,0} + \tilde{t}_i G_{n+2^i,0} t_i = (1 - t_{i-1}\tilde{t}_{i-1} - \tilde{t}_{i-1}t_{i-1})^{-1} t_{i-1}^2 \tilde{t}_i \\ &= (1 - t_{i-1}\tilde{t}_{i-1} - \tilde{t}_{i-1}t_{i-1})^{-1} \tilde{t}_{i-1}^2 \end{aligned} \quad (21)$$

Further we get:

$$\begin{aligned} &G_{10} = t_0 G_{00} + \tilde{t}_0 G_{20} \\ &G_{20} = t_1 G_{00} + \tilde{t}_1 G_{40} \\ &\vdots \\ &G_{2^n 0} = t_n G_{00} + \tilde{t}_n G_{2^{n+1}0} \end{aligned}$$

The iteration proceeds until $t_{n+1}, \tilde{t}_{n+1} < tol$. Collecting terms for G_{00} gives:

$$G_{10} = (t_0 + \tilde{t}_0 t_1 + \tilde{t}_0 \tilde{t}_1 t_2 + \cdots + \tilde{t}_0 \ldots \tilde{t}_{n-1} t_n) G_{00} = T G_{00} \quad (22)$$

Then substituting Eq. (22) into the 1st row of Eq. (19) yields

$$G_{00} = [zS_{00} - H_{00} - (H_{01} - zS_{01})T]^{-1} \quad (23)$$

Eq. (23) is the desired SGF of the right lead. One may note that it becomes the SGF of the left lead if H and S are replaced by their Hermitian. Therefore we can obtain the SGFs for the both leads simultaneously during one-time iteration.

A.2. Density of states $D_{L/R}(E)$

Consider an Bloch wave from the left lead ψ_n^L with energy E_n. The ballistic scattering state corresponding to ψ_n^L can be written as:

$$\psi_n = \begin{pmatrix} \psi_n^L + \tilde{\psi}_n^L \\ \psi_n^D \\ \psi_n^R \end{pmatrix} \quad (24)$$

where $\tilde{\psi}_n^L$ is the reflected wave, ψ_n^D is the part of the scattering state on the device and ψ_n^R is the transmitted wave. Then the Schrödinger equation for the whole open system is written as:

$$\begin{aligned} (E_n S - H)\psi_n &= \begin{pmatrix} E_n S_L - H_L & \tau_L^\dagger & 0 \\ \tau_L & E_n S_D - H_D & \tau_R \\ 0 & \tau_R^\dagger & E_n S_R - H_R \end{pmatrix} \begin{pmatrix} \psi_n^L + \tilde{\psi}_n^L \\ \psi_n^D \\ \psi_n^R \end{pmatrix} \\ &= 0 \Rightarrow (E_n S - H) \begin{pmatrix} \tilde{\psi}_n^L \\ \psi_n^D \\ \psi_n^R \end{pmatrix} \\ &= -\begin{pmatrix} E_n S_L - H_L & \tau_L^\dagger & 0 \\ \tau_L & E_n S_D - H_D & \tau_R \\ 0 & \tau_R^\dagger & E_n S_R - H_R \end{pmatrix} \begin{pmatrix} \psi_n^L \\ 0 \\ 0 \end{pmatrix} \end{aligned} \quad (25)$$

Since ψ_n^L is an eigenstate of the left lead, we have $(E_n S_L - H_L)\psi_n^L = 0$. Then Eq. (25) becomes:

$$E_nS - H)\begin{pmatrix}\tilde{\psi}_n^L\\ \psi_n^D\\ \psi_n^R\end{pmatrix} = \begin{pmatrix}0\\ -\tau_L\psi_n^L\\ 0\end{pmatrix} \tag{26}$$

Let $E_n \to E_n + i\eta$, $\eta \to 0^+$, assuming Eq. (26) still holds, we have

$$\begin{pmatrix}\tilde{\psi}_n^L\\ \psi_n^D\\ \psi_n^R\end{pmatrix} = G^R(E_n)\begin{pmatrix}0\\ -\tau_L\psi_n^L\\ 0\end{pmatrix} \tag{27}$$

Further, if $G^R(E_n)$ is partitioned as: [40]

$$G^R(E_n) = \begin{pmatrix}G_L^R & G_{LD}^R & G_{LR}^R\\ G_{DL}^R & G_D^R & G_{DR}^R\\ G_{RL}^R & G_{RD}^R & G_R^R\end{pmatrix}$$

Then we have

$$\psi_n^D = -G_D^R(E_n)\tau_L(E_n)\psi_n^L \tag{28}$$

Eq. (28) indicates that ψ_n^D can be considered as the output of a system formed by $G_D^R(E_n)$ and the coupling of the device with the left lead, τ_L, and the input is the Bloch wave of the left lead ψ_n^L.

Now we solve the density of states arising from the ψ_n^D. By definition we have:

$$D_L(E) = \sum_n \psi_n^D \psi_n^{D\dagger}\delta(E - E_n) \tag{29}$$

Substitute Eq. (28) into Eq. (29), one obtains:

$$\begin{aligned} D_L(E) &= \sum_n G_D^R\tau_L\psi_n^L\psi_n^{L\dagger}\tau_L^\dagger G_D^{R\dagger}\delta(E - E_n)\\ &= G_D^R\tau_L[\sum_n \psi_n^L\psi_n^{L\dagger}\delta(E - E_n)]\tau_L^\dagger G_D^A = G_D^R\tau_L D_L^L(E)\tau_L^\dagger G_D^A \end{aligned} \tag{30}$$

where $D_L^L(E)$ is the density of states on the left lead, and hence we have [40,43]

$$D_L^L(E) = \frac{i}{2\pi}(g_L^R - g_L^A) \tag{31}$$

Substitute Eq. (31) into Eq. (30) and it gives:

$$\begin{aligned} D_L(E) &= \frac{i}{2\pi}G_D^R\tau_L(g_L^R - g_L^A)\tau_L^\dagger G_D^A = \frac{i}{2\pi}G_D^R(\tau_L g_L^R\tau_L^\dagger - \tau_L g_L^A\tau_L^\dagger)G_D^A\\ &= \frac{i}{2\pi}G_D^R(\Sigma_L - \Sigma_L^\dagger)G_D^A = \frac{1}{2\pi}G_D^R\Gamma_L G_D^A \end{aligned} \tag{32}$$

Reference

[1] C.H. Shih, N.D. Chien, IEEE Electron Dev. Lett. 32 (2011) 1498–1500.
[2] M.L. Lee, E.A. Fitzgerald, M.T. Bulsara, M.T. Currie, A. Lochtefeld, J. Appl. Phys. 97 (2005).
[3] I. Ferain, C.A. Colinge, J.-P. Colinge, Nature 479 (2011) 310–316.
[4] D.K. Kim, Y. Lai, B.T. Diroll, C.B. Murray, C.R. Kagan, Nat. Commun. 3 (2012) 1216.
[5] Segal Michael, Nat. Nano (2008).
[6] L. Ding, Z. Zhang, S. Liang, T. Pei, S. Wang, Y. Li, W. Zhou, J. Liu, L.-M. Peng, Nat. Commun. 3 (2012) 677.
[7] S. Kim, A. Konar, W.-S. Hwang, J.H. Lee, J. Lee, J. Yang, C. Jung, H. Kim, J.-B. Yoo, J.-Y. Choi, Y.W. Jin, S.Y. Lee, D. Jena, W. Choi, K. Kim, Nat. Commun. 3 (2012) 1011.
[8] F. Schwierz, Nat. Nano 5 (2010) 487–496.
[9] F. Schwierz, Nat. Nano 6 (2011) 135–136.
[10] A. Javey, J. Guo, Q. Wang, M. Lundstrom, H. Dai, Nature 424 (2003) 654–657.
[11] T. Georgiou, R. Jalil, B.D. Belle, L. Britnell, R.V. Gorbachev, S.V. Morozov, Y.-J. Kim, A. Gholinia, S.J. Haigh, O. Makarovsky, L. Eaves, L.A. Ponomarenko, A.K. Geim, K.S. Novoselov, A. Mishchenko, Nat. Nano 8 (2013) 100–103.
[12] B. Radisavljevic, A. Radenovic, J. Brivio, V. Giacometti, A. Kis, NANO 6 (2011) 147–150.
[13] S. Iijima, Nature 354 (1991) 56–58.
[14] A.K. Geim, K.S. Novoselov, Nat. Mater. 6 (2007) 183–191.
[15] E.S. Penev, S. Bhowmick, A. Sadrzadeh, B.I. Yakobson, Nano Lett. 12 (2012) 2441–2445.
[16] A. Sadrzadeh, O.V. Pupysheva, A.K. Singh, B.I. Yakobson, J. Phys. Chem. A 112 (2008) 13679–13683.
[17] K.S. Novoselov, D. Jiang, F. Schedin, T.J. Booth, V.V. Khotkevich, S.V. Morozov, A.K. Geim, Proc. Natl. Acad. Sci. USA 102 (2005) 10451–10453.
[18] F. Xu, A. Sadrzadeh, Z. Xu, B.I. Yakobson, J. Appl. Phys. 114 (2013) 063714–063718.
[19] F. Xu, R. Li, J. Zhang, Z. Qian, Z. Shen, X. Zhao, S. Hou, Physica E 35 (2006) 168–172.
[20] C. Joachim, J.K. Gimzewski, A. Aviram, Nature 408 (2000) 541–548.
[21] M. Galperin, M.A. Ratner, A. Nitzan, A. Troisi, Science 319 (2008) 1056–1060.
[22] M.A. Reed, C. Zhou, C.J. Muller, T.P. Burgin, J.M. Tour, Science 278 (1997) 252–254.
[23] A.W. Ghosh, T. Rakshit, S. Datta, Nano Lett. 4 (2004) 565–568.
[24] S. Kubatkin, A. Danilov, M. Hjort, J. Cornil, J.-L. Bredas, N. Stuhr-Hansen, P. Hedegard, T. Bjornholm, Nature 425 (2003) 698–701.
[25] B. Xu, N.J. Tao, Science 301 (2003) 1221–1223.
[26] I.G. Salfij, NANO 5 (2010) 737–741.
[27] H. Song, Y. Kim, Y.H. Jang, H. Jeong, M.A. Reed, T. Lee, Nature 462 (2009) 1039–1043.
[28] J. Park, A.N. Pasupathy, J.I. Goldsmith, C. Chang, Y. Yaish, J.R. Petta, M. Rinkoski, J.P. Sethna, H.D. Abruna, P.L. McEuen, D.C. Ralph, Nature 417 (2002) 722–725.
[29] W. Liang, M.P. Shores, M. Bockrath, J.R. Long, H. Park, Nature 417 (2002) 725–729.
[30] A.A. Farajian, R.V. Belosludov, H. Mizuseki, Y. Kawazoe, T. Hashizume, B.I. Yakobson, J. Chem. Phys. 127 (2007) 024901–024905.
[31] F. Léonard, J. Tersoff, Phys. Rev. Lett. 85 (2000) 4767–4770.
[32] B.J. van Wees, H. van Houten, C.W.J. Beenakker, J.G. Williamson, L.P. Kouwenhoven, D. van der Marel, C.T. Foxon, Phys. Rev. Lett. 60 (1988) 848–850.
[33] R. Saito, G. Dresselhaus, M.S. Dresselhaus, Physical Properties of Carbon Nanotubes, Imperial College Press, London, 1998.
[34] E. Artacho, E. Anglada, O. Dieguez, J.D. Gale, A. Garcia, J. Junquera, R.M. Martin, P. Ordejon, J.M. Pruneda, D. Sanchez-Portal, J.M. Soler, J. Phys. Condens. Matter 20 (2008).
[35] J.-L. Calais, Int. J. Quantum Chem. 47 (1993) 101.
[36] R.M. Dreizler, E.K.E.K.U. Gross, Density Functional Theory: An Approach to the Quantum Many-Body Problem, Springer-Verlag, 1990.
[37] K. Hirose, First-principles Calculations in Real-space Formalism: Electronic Configurations and Transport Properties of Nanostructures, Imperial College Press, 2005.
[38] Y.Q. Xue, S. Datta, M.A. Ratner, Chem. Phys. 281 (2002) 151–170.
[39] Y.Q. Xue, S. Datta, M.A. Ratner, J. Chem. Phys. 115 (2001) 4292–4299.
[40] S. Datta, Electronic Transport in Mesoscopic Systems, Cambridge University Press, 1997.
[41] K.K. Paulla, A.A. Farajian, J. Phys. Chem. C 117 (2013) 12815–12825.
[42] Y. Meir, N.S. Wingreen, Phys. Rev. Lett. 68 (1992) 2512–2515.
[43] R. Li, J. Zhang, S. Hou, Z. Qian, Z. Shen, X. Zhao, Z. Xue, Chem. Phys. 336 (2007) 127–135.
[44] T.N. Todorov, J. Phys.: Condens. Matter 14 (2002) 3049–3084.
[45] H.U. Baranger, A.D. Stone, Phys. Rev. B 40 (1989) 8169–8193.
[46] S. Datta, Electron Transport in Mesoscopic Systems, Cambridge University Press, Cambridge, 1995.
[47] S. Datta, Phys. Rev. B 45 (1992) 1347–1362.
[48] W. Landgraf, S. Shallcross, K. Türschmann, D. Weckbecker, O. Pankratov, Phys. Rev. B 87 (2013) 075433.
[49] M.S. Tang, C.Z. Wang, C.T. Chan, K.M. Ho, Phys. Rev. B 53 (1996) 979–982.
[50] M.L. Elert, C.T. White, Phys. Rev. B 28 (1983) 7387–7389.
[51] M.L. Elert, C.T. White, J.W. Mintmire, Mol. Cryst. Liq. Cryst. 125 (1985) 329–335.
[52] M.L. Elert, C.T. White, Macromolecules 20 (1987) 1411–1414.
[53] C.T. White, D.H. Robertson, J.W. Mintmire, Phys. Rev. B 47 (1993) 5485–5488.
[54] J.W. Mintmire, C.T. White, Carbon 33 (1995) 893–902.
[55] C.T. White, J.W. Mintmire, J. Phys. Chem. B 109 (2004) 52–65.
[56] D. Gunlycke, H.M. Lawler, C.T. White, Phys. Rev. B 77 (2008) 014303.
[57] V.N. Popov, V.E. Van Doren, M. Balkanski, Phys. Rev. B 59 (1999) 8355–8358.
[58] V.N. Popov, Phys. Rev. B 67 (2003).
[59] E. Bichoutskaia, A.M. Popov, A. El-Barbary, M.I. Heggie, Y.E. Lozovik, Phys. Rev. B 71 (2005) 113403.
[60] V.N. Popov, L. Henrard, P. Lambin, Phys. Rev. B 72 (2005) 035436.
[61] D.-B. Zhang, M. Hua, T. Dumitrica, J. Chem. Phys. 128 (2008) 084104.
[62] M.S. Miao, M.L. Zhang, V.E. Van Doren, J.J. Ladik, J.W. Mintmire, J. Phys. Chem. A 104 (2000) 6809–6816.
[63] P. Koskinen, Appl. Phys. Lett. 99 (2011).
[64] O.O. Kit, T. Tallinen, L. Mahadevan, J. Timonen, P. Koskinen, Phys. Rev. B 85 (2012) 085428.
[65] T.W. Chamberlain, J. Biskupek, G.A. Rance, A. Chuvilin, T.J. Alexander, E. Bichoutskaia, U. Kaiser, A.N. Khlobystov, ACS Nano 6 (2012) 3943–3953.
[66] E. Akatyeva, T. Dumitrică, Phys. Rev. Lett. 109 (2012) 035501.
[67] D.B. Zhang, T. Dumitrică, Phys. Rev. B 85 (2012) 035445.
[68] S.M. Avdoshenko, P. Koskinen, H. Sevinçli, A.A. Popov, C.G. Rocha, Sci. Rep. 3 (2013).
[69] P.J. Lin-Chung, A.K. Rajagopal, J. Phys. Condens. Matter 6 (1994) 3697.
[70] A. Sadrzadeh, M. Hua, B.I. Yakobson, Appl. Phys. Lett. 99 (2011) 013102–013103.
[71] R. Rurali, E. Hernández, Comput. Mater. Sci. 28 (2003) 85–106.
[72] D.A. Papaconstantopoulos, M.J. Mehl, J. Phys. Condens. Matter 15 (2003) R413.

[73] J.C. Slater, G.F. Koster, Phys. Rev. 94 (1954) 1498–1524.
[74] X. Zhao, Y. Ando, Y. Liu, M. Jinno, T. Suzuki, Phys. Rev. Lett. 90 (2003) 187401.
[75] Y.P. Kudryavtsev, R.B. Heimann, S.E. Evsyukov, J. Mater. Sci. 31 (1996) 5557–5571.
[76] A.K. Nair, S.W. Cranford, M.J. Buehler, EPL (Europhys. Lett.) 95 (2011) 16002.
[77] Y.-W. Son, M.L. Cohen, S.G. Louie, Nature 444 (2006) 347–349.
[78] A.H. Castro Neto, F. Guinea, N.M.R. Peres, K.S. Novoselov, A.K. Geim, Rev. Mod. Phys. 81 (2009) 109–162.
[79] D.A. Areshkin, D. Gunlycke, C.T. White, Nano Lett. 7 (2006) 204–210.
[80] D.A. Areshkin, C.T. White, Nano Lett. 7 (2007) 3253–3259.
[81] A. Kletsov, Y. Dahnovsky, J.V. Ortiz, J. Chem. Phys. 126 (2007) 134105.
[82] A.A. Farajian, R.V. Belosludov, H. Mizuseki, Y. Kawazoe, Thin Solid Films 499 (2006) 269–274.
[83] M.P.L. Sancho, J.M.L. Sancho, J. Rubio, J. Phys. F: Met. Phys. 14 (1984) 1205.